Geophysical Prospecting

EAGE EUROPEAN ASSOCIATION OF GEOSCIENTISTS & ENGINEERS

Geophysical Prospecting, 2019, **67**, 2332–2342 doi: 10.1111/1365-2478.12839

3D waveform inversion of downhole microseismic data for transversely isotropic media

Oscar Jarillo Michel* and Ilya Tsvankin*

Center for Wave Phenomena, Colorado School of Mines, Golden, CO 80401, USA

Received March 2019, revision accepted June 2019

ABSTRACT

3D anisotropic waveform inversion could provide high-resolution velocity models and improved event locations for microseismic surveys. Here we extend our previously developed 2D inversion methodology for microseismic borehole data to 3D transversely isotropic media with a vertical symmetry axis. This extension allows us to invert multicomponent data recorded in multiple boreholes and properly account for vertical and lateral heterogeneity. Synthetic examples illustrate the performance of the algorithm for layer-cake and 'hydraulically fractured' (i.e. containing anomalies that simulate hydraulic fractures) models. In both cases, waveform inversion is able to reconstruct the areas which are sufficiently illuminated for the employed source-receiver geometry. In addition, we evaluate the sensitivity of the algorithm to errors in the source locations and to band-limited noise in the input displacements. We also present initial inversion results for a microseismic data set acquired during hydraulic fracturing in a shale reservoir.

Key words: Anisotropy, Transverse isotropy, Multicomponent, Full-waveform inversion, Microseismic.

INTRODUCTION

Microseismic data have been widely used to monitor hydraulic fracturing in unconventional shale plays (e.g. Maxwell 2014; Grechka and Heigl 2017). Knowledge of the fracture geometry and evolution is essential in optimizing stimulation operations and refining reservoir models. Microseismic event location requires an accurate velocity model, which typically has to include anisotropy because shales are at least transversely isotropic (TI) or may have a lower symmetry (e.g. due to natural or induced fracturing). Source locations can be estimated simultaneously with the velocity field using joint anisotropic inversion of direct-arrival traveltimes of P-waves and split S-waves (Grechka and Yaskevich 2013, 2014). Recently, Grechka *et al.* (2017) carried out high-resolution Kirchhoff migration of microseismic borehole data and interpreted the identified 'geobodies' as hydraulic fractures produced during reservoir stimulation.

As discussed in Maxwell (2014), Grechka and Heigl (2017) and Jarillo Michel and Tsvankin (2015, 2017), waveform inversion (WI) is a promising tool for high-resolution velocity analysis and event location from microseismic data. Recently, it has been shown that WI of passive seismic data can help recover the source location, origin time and seismic moment tensor (Kim, Liu and Tromp 2011; Jarillo Michel and Tsvankin 2015), as well as build 2D anisotropic models (Jarillo Michel and Tsvankin 2017). The main benefit of WI is an increase in parameter resolution achieved by incorporating phase and amplitude information into the data-fitting procedure. The WI gradient can be efficiently computed with just two modelling simulations using the adjoint-state method (Fichtner, Bunge and Igel 2006; Plessix 2006; Kamath, Tsvankin and Díaz 2017).

3D elastic anisotropic WI, however, involves several challenges that so far have prevented its successful application

*E-mail: ojarillo@mymail.mines.edu, ilya@mines.edu

to microseismic data. The average frequency of microseismic events is on the order of several hundred Hertz, which requires fine sampling in space and time for accurate wave-equation-based modelling. This increases the storage and computing-time requirements for finite-difference and finite-element algorithms. Traditionally, most wavefield extrapolators for WI applications are based on finite-difference schemes, which suffer from numerical dispersion for events with high-frequency content. Pseudospectral methods (Cheng *et al.* 2016; Sun *et al.* 2016) provide a viable alternative to finite differences because they mitigate dispersion without the need to reduce the grid size.

Another challenge in applying 3D WI to microseismic data is the limited source-receiver coverage (data aperture). Microseismic events are usually acquired by multicomponent geophones placed in a single or, in the best-case scenario, several vertical monitor wells. Microseismic data recorded by surface arrays usually are more noisy and the corresponding source-receiver geometries emphasize near-vertical propagation, which is less favourable for imaging hydraulic fractures, building velocity models (particularly anisotropic) and estimating source moment tensors. Grechka and Duchkov (2011) study the feasibility of resolving anisotropic velocity fields from the traveltimes of microseismic events recorded with limited angle coverage.

Here, we extend the 2D WI methodology presented in Jarillo Michel and Tsvankin (2017) to 3D velocity inversion of borehole microseismic data from TI media with a vertical symmetry axis (VTI). The extension includes 3D modelling of elastic wave propagation using a pseudospectral technique as well 3D computation of the inversion gradient with the adjoint-state method. The algorithm is designed to reconstruct 3D VTI velocity models under the assumption that the source parameters have been estimated (e.g. by traveltime inversion).

We start by describing the inversion methodology including the forward-modelling technique and computation of the inversion gradient. Then the algorithm is tested on multicomponent synthetic data recorded along several vertical 'boreholes' embedded in a layered VTI medium. That model is also used to evaluate the sensitivity of the inverted parameters to errors in the source locations and to band-limited random noise. Next, we present a synthetic inversion example for a model that includes local parameter anomalies simulating hydraulic fractures. Finally, in combination with moment-tensor inversion, we perform WI of microseismic data acquired in a vertical well during hydraulic stimulation at an unconventional shale reservoir. Although the method could potentially operate with the entire seismogram, the accuracy of the initial velocity field is sufficient for matching the waveforms of only the direct arrivals.

WAVEFORM-INVERSION METHODOLOGY

The general design of the 3D waveform-inversion (WI) algorithm is similar to the 2D implementation discussed by Jarillo Michel and Tsvankin (2017). However, the extension of the method to 3D is necessary to properly handle lateral heterogeneity, as well as acquisition geometries typical for microseismic surveys. The 3D wavefield extrapolation is performed here using a pseudospectral approach instead of finite-differences. The elastic wave equation for a point source in a heterogeneous anisotropic medium can be written as

$$\rho \frac{\partial^2 u_i}{\partial t^2} - \frac{\partial}{\partial x_j}\left(c_{ijkl}\frac{\partial u_k}{\partial x_l}\right) = -M_{ij}\frac{\partial[\delta(\mathbf{x}-\mathbf{x}^s)]}{\partial x_j}S(t), \quad (1)$$

where $\mathbf{u}(\mathbf{x}, t)$ is the displacement field, t is time, c_{ijkl} is the stiffness tensor ($i, j, k, l = 1, 2, 3$), $\rho(\mathbf{x})$ is the density, $\mathbf{M}$ is the source moment tensor, $\mathbf{x}^s$ is the source location, $S(t)$ is the source signal and $\delta(\mathbf{x} - \mathbf{x}^s)$ is the spatial δ-function; summation over repeated indices is implied. Pseudospectral methods compute the spatial derivatives of the wavefield $\mathbf{u}(\mathbf{x}, t)$ in the frequency-wavenumber domain and the temporal derivatives of $\mathbf{u}(\mathbf{x}, t)$ with finite differences using forward time-stepping (Cheng *et al.* 2016).

The data residuals are quantified by the conventional l_2-norm objective function:

$$\mathcal{F}(\mathbf{m}) = \frac{1}{2}\sum_{n=1}^{N}\|\mathbf{d}_{\text{pre}}(\mathbf{m}) - \mathbf{d}_{\text{obs}}\|^2, \quad (2)$$

where $\mathbf{d}_{\text{obs}}$ is the observed displacement and $\mathbf{d}_{\text{pre}}(\mathbf{m})$ is the displacement simulated for the trial model $\mathbf{m}$. The wavefield produced by each microseismic event is recorded by N receivers located at $\mathbf{x}^{r_n}$ ($n = 1, 2, \ldots, N$); summation over the available sources is implied.

The current version of the algorithm is designed to estimate the spatially varying vertical symmetry axis (VTI) parameters without *a priori* assumptions about the model structure using known source locations, moment tensors and origin times. The parameterization includes the P-wave horizontal velocity (V_{hor}), S-wave vertical velocity (V_{S0}), anellipticity coefficient η and Thomsen parameter ε, which are specified on a rectangular grid. This choice of parameters helps reduce trade-offs in WI, in particular when waves travel mostly near the horizontal direction (Alkhalifah and Plessix 2014; Kamath *et al.* 2017).

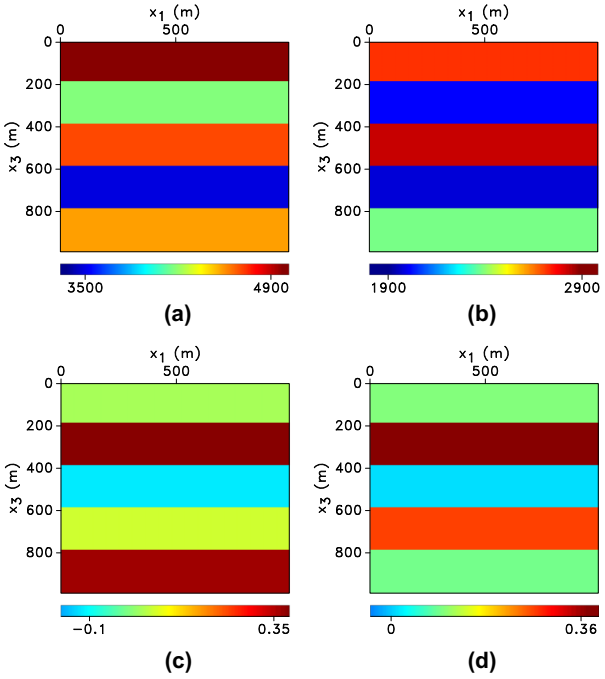

Figure 1 Parameters of a layered VTI medium: (a) V_{hor}, (b) V_{S0}, (c) η and (d) ε (velocities are in m/s). The grid size is 10 m.

The gradient of the objective function with respect to the medium parameters is obtained using the adjoint-state method. The derivatives of the objective function with respect to the stiffness coefficients c_{ijkl} are given by Liu and Tromp (2006), Jarillo Michel and Tsvankin (2017) and Kamath *et al.* (2017):

$$\frac{\partial \mathcal{F}}{\partial c_{ijkl}} = -\int_0^T \frac{\partial u_i}{\partial x_j}\frac{\partial \psi_k}{\partial x_l}, \tag{3}$$

where $\mathbf{u}$ and $\boldsymbol{\psi}$ are the forward and adjoint displacement fields, respectively. Closed-form 3D expressions for the inversion gradient can be found in the Appendix. Model updating is performed with the *l*–BFGS (*limited–memory*–Broyden–Fletcher–Goldfarb–Shanno) method (Byrd *et al.* 1995), which approximates the inverse of the Hessian matrix using the objective-function gradient computed for several previous iterations.

SYNTHETIC EXAMPLES OF 3D VELOCITY INVERSION

Horizontally layered model

First, we test the 3D waveform-inversion (WI) algorithm on the layered vertical symmetry axis (VTI) model from Fig. 1. Although the medium is laterally homogeneous and could be handled by 2D inversion (Jarillo Michel and Tsvankin 2017), we do not assume that the model structure is known and estimate the VTI parameters on a 3D grid. The data are generated by a tight cloud of 30 dislocation-type microseismic sources whose parameters are fixed at the actual values, and recorded by multicomponent receivers placed in three vertical 'boreholes' (Fig. 2). The initial model for all parameters is obtained by smoothing the actual fields in the vertical direction, with additional parameter distortions in the middle layer. Due to the limited azimuthal source-receiver coverage, accurate velocity updates are largely restricted to the central part of the model.

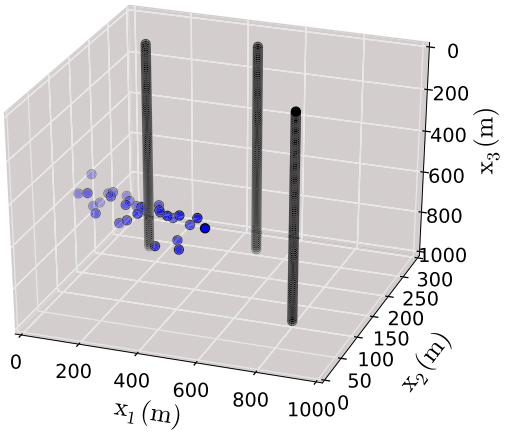

Figure 2 Microseismic sources (blue dots) and three vertical 'boreholes' with the receiver arrays (black lines) for the model in Fig. 1. The boreholes are placed at the following locations: (x_1 = 150 m, x_2 = 220 m), (x_1 = 500 m, x_2 = 250 m) and (x_1 = 800 m, x_2 = 100 m), with the receivers positioned at each grid point. All events represent dip-slip sources with a horizontal fault plane (dip angle $\theta = 0°$). The central frequency of the source signal is 60 Hz.

After 15 iterations, the algorithm was able to reconstruct all four parameters in the middle layer with acceptable accuracy (Fig. 3) despite sparse data coverage. However, parameter updates in the other layers are unsatisfactory due to insufficient illumination. Resolving ε in this parameterization requires better illumination near the vertical direction, as discussed by Alkhalifah and Plessix (2014) and Jarillo Michel and Tsvankin (2017). The reconstructed 3D fields of the velocities V_{hor} and V_{S0} and of the coefficient η generally reproduce the actual layered structure (Fig. 4).

Influence of errors in source locations and noise

It is also important to test the sensitivity of the algorithm to errors in the source locations. We reduced the actual x_1-coordinates of all events for the model in Fig. 1 by 15 m,

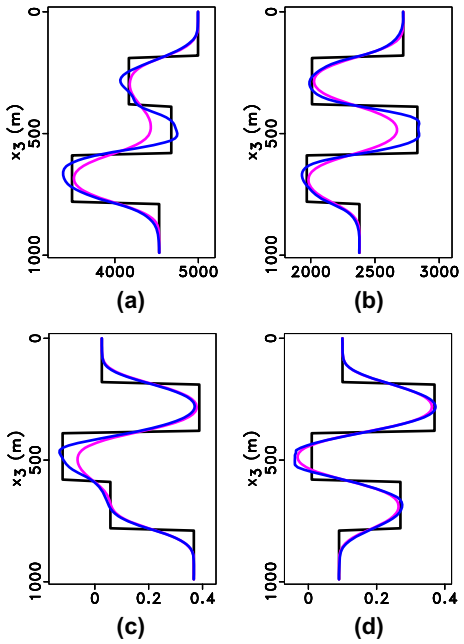

Figure 3 Vertical profiles of the actual (black), initial (magenta) and inverted (blue) VTI parameters (after 15 iterations) for the model in Fig. 1: (a) V_{hor}, (b) V_{S0}, (c) η and (d) ε (velocities are in m/s). The profiles are plotted at ($x_1 = 400$ m, $x_2 = 130$ m).

while fixing the coordinates x_2 and x_3 at the actual values. Such location errors generally exceed those produced by anisotropic traveltime inversion of microseismic data (V. Grechka, pers. comm.). Although there are some distortions in the interval parameters for several layers (particularly where the data coverage is sparse), the inversion results are still satisfactory (Fig. 5).

Next, we add random Gaussian noise (its average magnitude is close to 10% of the maximum S-wave amplitude) in the frequency band of the signal to the observed displacements for the model in Fig. 1. Despite the significant magnitude of the noise, it does not completely mask the arrivals (Fig. 6). The noise causes some deterioration in the inversion results in several layers but the V_{hor}- and η-fields are reconstructed with acceptable accuracy (Fig. 7).

Model with 'hydraulic fractures'

By migrating field microseismic data, Grechka *et al.* (2017) identify 'geobodies' representing hydraulic fractures at different stages of well stimulation. In the model from Fig. 8, we introduce two anomalies in all four VTI parameters which could emulate hydraulic fractures.

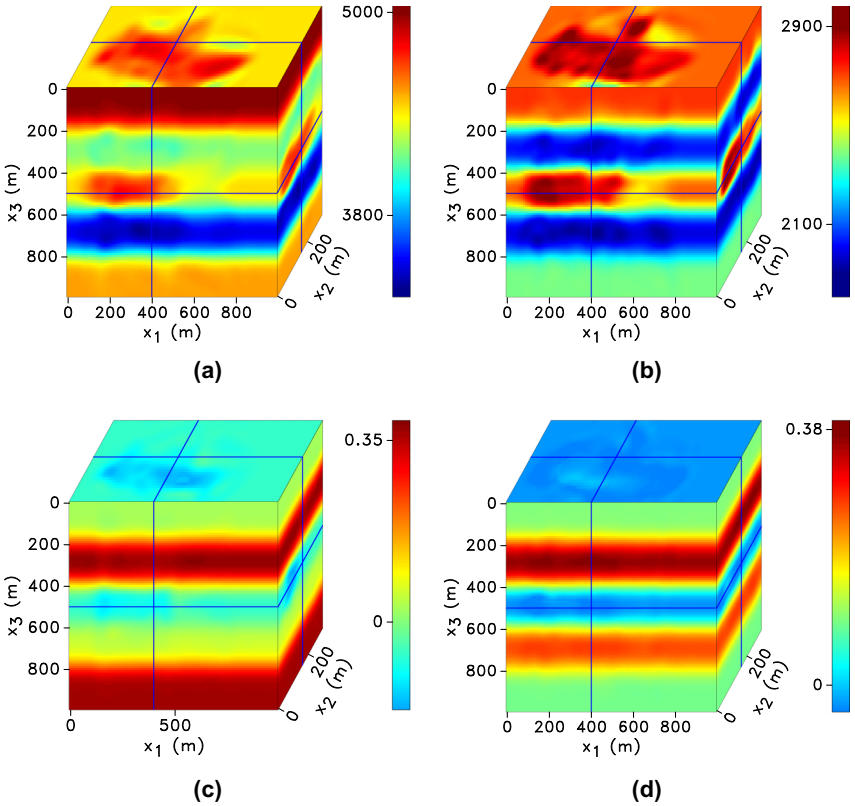

Figure 4 3D fields of the inverted parameters: (a) V_{hor}, (b) V_{S0}, (c) η and (d) ε (velocities are in m/s). The sides of the models here and on subsequent plots show the parameters in the orthogonal planes marked by the blue lines.

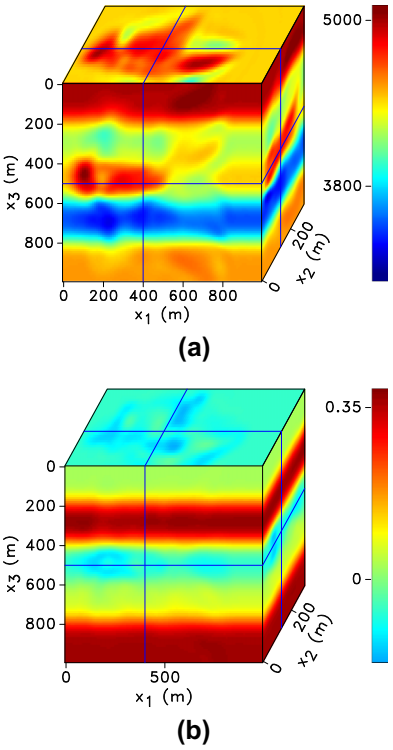

Figure 5 (a) Inverted velocity V_{hor} (in m/s) and (b) the coefficient η for the model in Fig. 1. The x_1-coordinates of all events used in the inversion are reduced by 15 m from the actual values.

We use the source-receiver geometry in Fig. 2, where the microseismic events are assumed to occur in the vicinity of a 'horizontal stimulation well'. The initial model for all parameters is obtained by smoothing their actual fields (without including the anomalies) in the vertical direction; the source parameters are fixed at the actual values. After 15 iterations of WI, the two 'fractures' can be reliably identified in the V_{hor}- and V_{S0}-fields (Fig. 9).

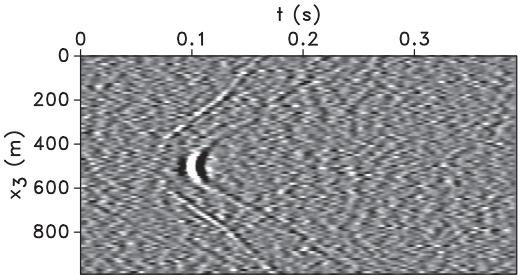

Figure 6 Vertical displacement contaminated by Gaussian noise in the borehole located at ($x_1 = 500$ m, $x_2 = 250$ m) for the model in Fig. 1.

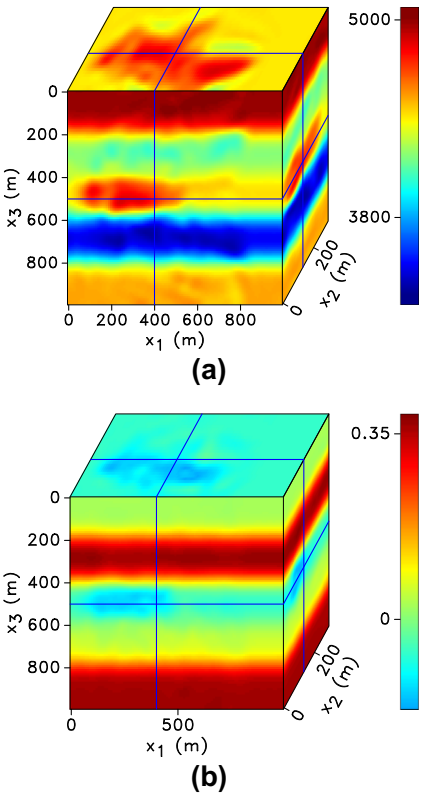

Figure 7 3D fields of the inverted velocity (a) V_{hor} and (b) the coefficient η for the model in Fig. 1. The data are contaminated by Gaussian noise (see Fig. 6).

APPLICATION TO FIELD DATA

The microseismic survey used here was recorded to test engineering parameters for hydraulic fracturing at an unconventional shale reservoir. The data set contains more than 900 located microseismic events triggered during hydraulic well stimulation. The section is mainly composed of five formations: the limestone (LP), upper shales (UB), middle sandstones and siltstones (MB), lower shales (LB) and dolomites (TF) (Table 1).

Conventional processing of the microseismic events was carried out by the service company that acquired the data. The events were originally located using a horizontally layered isotropic velocity model obtained from sonic logs, perforation shots and sleeve-opening information. The isotropic model, however, proved to be insufficient for accurate event location, and cores collected in the LB shale exhibit strong velocity anisotropy. The initial layered anisotropic velocity model and the source coordinates and origin times were obtained using traveltime picks of the direct P-, S_1- and S_2-waves recorded in two monitor wells.

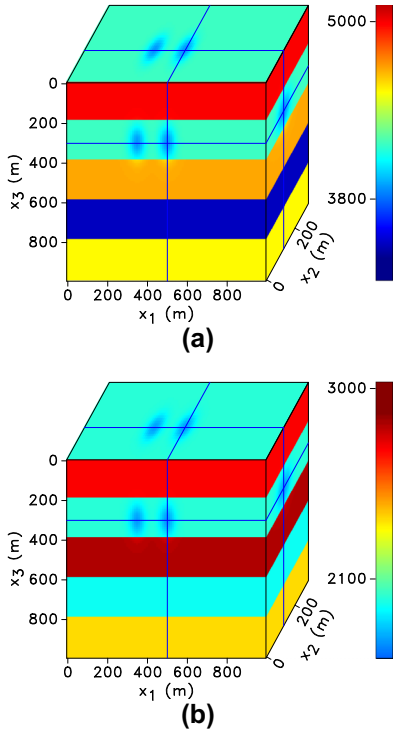

Figure 8 3D fields of the velocities (a) V_{hor} and (b) V_{S0} (in m/s). Two Gaussian anomalies simulating hydraulic fractures are embedded in the second layer.

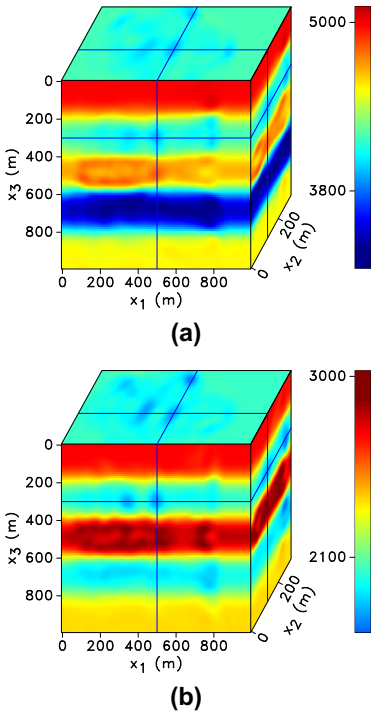

Figure 9 3D fields of the inverted velocities (a) V_{hor} and (b) V_{S0} (in m/s) for the model in Fig. 8.

Table 1 Parameters of five layers (LP, UB, MB, LB and TF) comprising the section. The top three layers (LP, UB, MB) were found to be triclinic but the table lists the closest VTI model for each layer. The layer thicknesses are shown in Fig. 11

Layer	V_{P0} (m/s)	V_{S0} (m/s)	ε	δ	γ	ρ (g/cm^3)
LP	4560	2720	0.10	0.07	0.02	2660
UB	3160	2010	0.37	−0.01	0.33	2660
MB	4630	2830	0.01	0.17	−0.12	2640
LB	2810	1970	0.27	0.19	0.35	2610
TF	4170	2380	0.09	0.16	0.13	2300

DATA PROCESSING

Data conditioning is an essential prerequisite for successful waveform inversion (WI) of microseismic data. We start by discussing the preprocessing sequence applied to this data set. The majority of microseismic events occur in the limestone (LP) formation, about 150 m above the stimulation well. Event registration was performed in two near-vertical monitor wells, one of which (well 'A' with 14 receivers) is used here (Fig. 10). To test the inversion algorithm, we start by processing only the direct P-wave arrivals. Unfortunately, the accuracy of the initial velocity model (Table 1 and Fig. 11) is insufficient for reproducing the coda formed by multiples, scattered waves, etc.

3D WI of microseismic data requires application of several preprocessing steps. Typical microseismic records have a relatively small signal-to-noise ratio, which causes problems in identifying low-amplitude P-waves. We selected 14

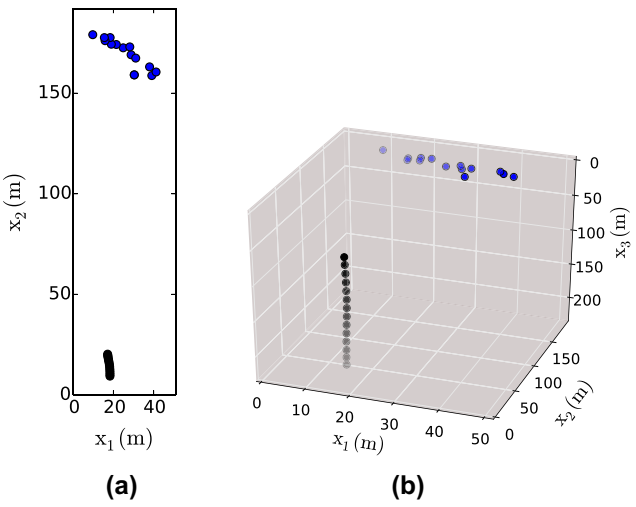

Figure 10 Sources (blue dots) and receivers (black dots) for the field data set (Table 1): (a) map view and (b) 3D plot.

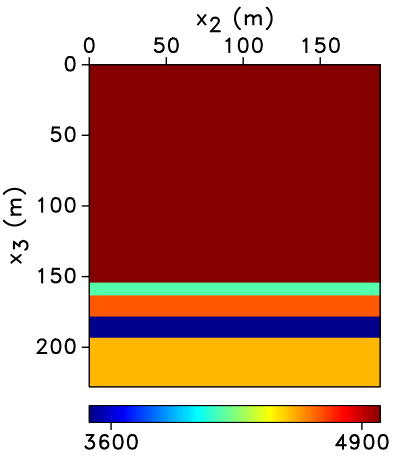

Figure 11 Initial velocity V_{hor} (in m/s) obtained by traveltime inversion of the field data (see Table 1).

microseismic events that produce P-wave direct arrivals whose amplitude is sufficient for reliable picking (Fig. 12a). For some of the chosen events, these arrivals could not be picked on all displacement components. To enhance the signal, we applied low-pass and adaptive filters to remove high-frequency and periodic noise, respectively (Fig. 12b). The adaptive filter is based on the Fourier transform of the autocorrelation of a noise window (Wuestefeld *et al.* 2010).

Wavefield simulation for WI requires knowledge of the source wavelet, which has to be obtained from the field data. To estimate the wavelet for each microseismic event, we stacked the traces along the P-wave moveout curve (Fig. 13a). The stack is performed separately for each displacement component and the wavelet is computed as the average over the stacked signals (Fig. 13b).

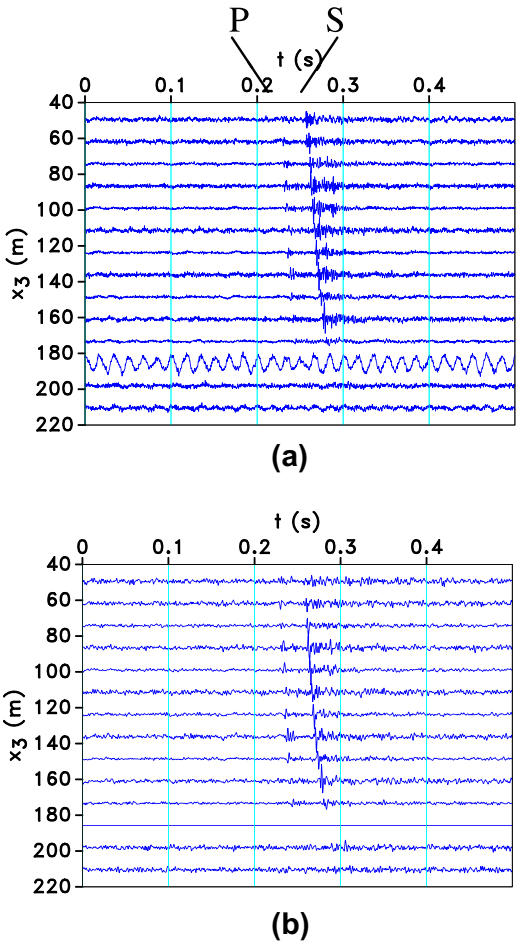

Figure 12 (a) Vertical displacement of a microseismic event recorded in well A. Direct P- and S-wave arrivals (marked) are visible on most traces. (b) The section from plot (a) after low-pass (the cut-off frequency is 500 Hz) and adaptive filtering. Due to its low signal-to-noise ratio, one of the traces has been removed.

Estimation of moment tensor

Information about the source mechanism is crucial for waveform inversion (WI) of microseismic data (Kim *et al.* 2011; Jarillo Michel and Tsvankin 2015). The observed displacement from a point source at geophone location $\mathbf{x}_r$ can be represented as (Aki and Richards 2002):

$$u_n^{(\mathbf{x}_r)} = M_{pq} * G_{np,q}^{(\mathbf{x}_r,\mathbf{x}_s)}, \tag{4}$$

where u_n is the nth displacement component ($n = 1, 2, 3$), $M_{pq} = \tilde{M}_{pq} M_0(t)$ is the time-dependent seismic moment tensor and $G_{np,q}$ are the derivatives of Green's function G_{np} with respect to the source coordinates $x_{s,q}$, and $*$ denotes temporal convolution summation over repeated indices is implied.

Following Vavryčuk and Kühn (2012), equation (4) can be applied to the amplitudes of the direct arrivals. The time-dependent derivatives $G_{np,q}$ in equation (4) are replaced with the maximum amplitudes of the corresponding events, which allows us to invert for the matrix $\tilde{M}_{pq}$ instead of M_{pq}.

To estimate the moment tensor, we solve the linear inverse problem in equation (4) by the least-squares method (Stump and Johnson 1977; Jost and Herrmann 1989; Vavryčuk and Kühn 2012):

$$\tilde{\mathbf{M}} = (\tilde{\mathbf{G}}^{\mathrm{T}} \tilde{\mathbf{G}})^{-1} \tilde{\mathbf{G}}^{\mathrm{T}} \mathbf{u}, \tag{5}$$

where $\tilde{\mathbf{G}}$ is the matrix containing Green's function derivatives $G_{np,q}$ (as mentioned above, we pick just the event amplitudes on the seismograms of $G_{np,q}$). The synthetic Green's functions

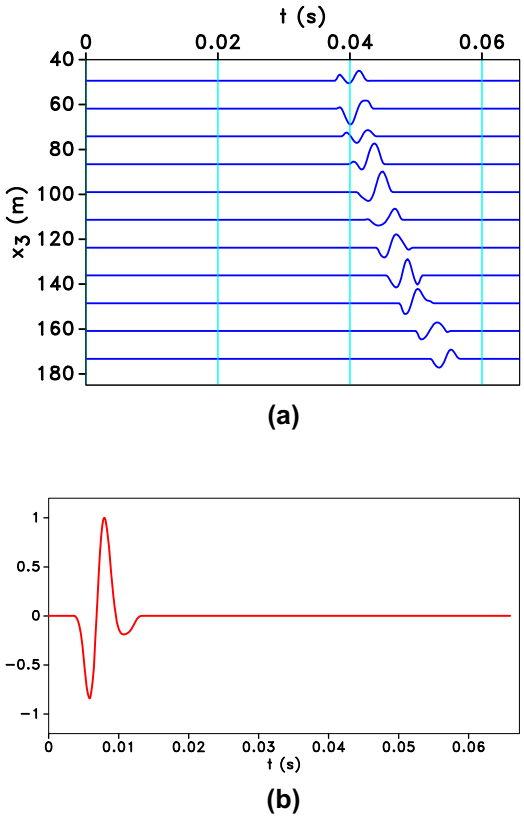

Figure 13 (a) Vertical displacement from Fig. 12(a) windowed to include just the direct P-wave arrival. The three bottom traces have been removed because they did not contain identifiable direct P-waves. Wavelet estimation is performed by stacking along the event moveout. To better visualize the arrivals, the time axis differs from the one in Fig. 12(a). (b) P-wavelet estimated after stacking and averaging windowed displacement components from plot (a).

and their spatial derivatives are generated by the pseudospectral method for the initial velocity model (Sun *et al.* 2016). The data exhibit shear-wave splitting, and we combine P-waves with the direct SH-arrivals recorded on the transverse displacement component in estimating $\tilde{\mathbf{M}}$. Although SV-waves can be identified on the vertical component, they are too noisy to be used in moment-tensor inversion.

The tensor $\tilde{\mathbf{M}}$ is obtained by substituting the amplitudes of the direct P- and SH-waves into equation (5) (Fig. 14). In general, P- and SH-wave amplitudes do not provide enough information to uniquely recover the full moment tensor, unless the data are recorded in several boreholes (Vavryčuk 2007). However, the estimated moment tensor proved to be sufficient to match the input data (the direct P- and SH-wave amplitudes) for this source-receiver configuration.

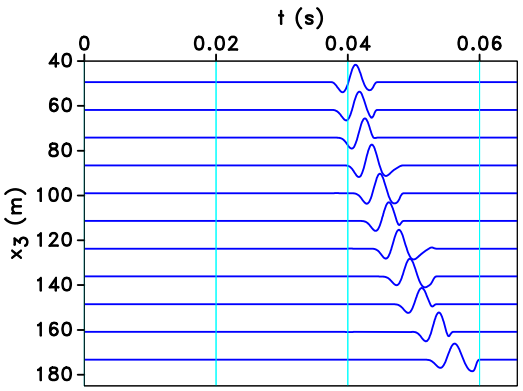

Figure 14 Windowed vertical displacement for the event from Fig. 12(a) obtained using pseudospectral modelling with the estimated moment tensor **M** (compare with Fig. 13a). To better visualize the arrivals, the time axis differs from the one in Fig. 12(a).

Waveform inversion

As an initial test of the WI algorithm, we carry out inversion of the P-wave direct arrivals for the horizontal velocity V_{hor} and the anellipticity coefficient η. The parameters V_{hor} and η can be constrained using P-waves propagating in near-horizontal directions (Alkhalifah and Plessix 2014). The initial parameters are obtained by vertical smoothing of the model from Fig. 11. Figure 15 shows a snapshot of the wavefield computed for one of the microseismic events with the initial velocity model.

After 13 iterations of waveform inversion for the velocity V_{hor}, the objective function is substantially reduced (Fig. 16).

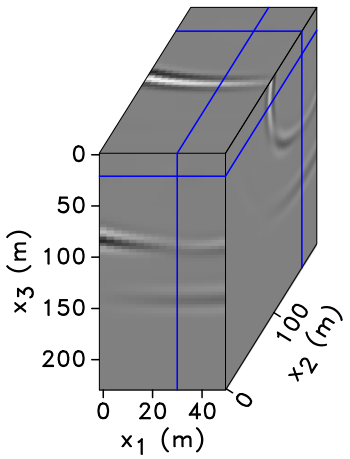

Figure 15 Wavefield snapshot at 0.035 s computed for one of the microseismic events in Fig. 10 using the initial velocity model. The sides show the wavefield in the planes marked by the blue lines. The event is located at the intersection of these planes. The grid size is 3 m.

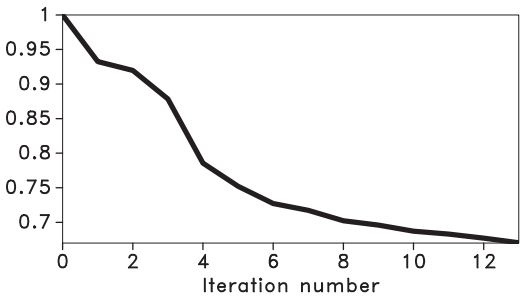

Figure 16 Change of the normalized objective function with iterations for the field data. The inversion was performed just for the velocity V_{hor}, with the other parameters fixed at the initial values.

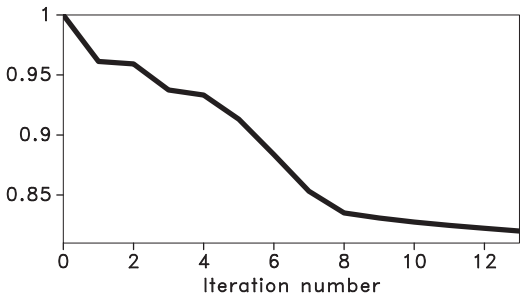

Figure 18 Change of the normalized objective function with iterations for the field data. The inversion was performed just for the parameter η with the updated V_{hor}.

Figure 17 shows that the model-updating algorithm somewhat increased V_{hor} in the area illuminated by the available microseismic events. The seismograms computed with the inverted V_{hor}-model provide a better match to the observed data (direct P-waves). Next, the updated field of V_{hor} is used to invert for the coefficient η, which further reduces the objective function (Fig. 18) and improves data fitting (Fig. 19). We expect to obtain higher resolution results after adding more events and including S-waves in the inversion.

DISCUSSION

Although both synthetic and field-data results discussed above look promising, there are many challenges in making waveform inversion standard for microseismic applications. First, the data coverage and illumination have to be sufficient for constraining all pertinent model parameters. Second, the signal-to-noise ratio for at least the first arrivals has to be high enough for using their waveforms. Third, waveform inversion requires reasonably accurate initial estimates of the velocity field and event coordinates. Fourth, the issue of parameter trade-offs (especially between the velocity parameters and event locations) requires further study, especially for realistic anisotropic models.

Note that partial compensation for suboptimal illumination can be achieved by applying gradient conditioning and inversion regularization methods. The problems of cycle-skipping and insufficient accuracy of the initial velocity model and source parameters can be addressed using a multiscale inversion approach and/or applying alternative objective functions that have been explored in waveform-inversion (WI) algorithms for surface seismic data.

Including both P- and S-waves in waveform inversion is highly beneficial in refining the locations of microseismic sources and estimating the medium parameters. Although shear waves are generally more difficult to process for WI purposes than compressional waves, S-wave information is

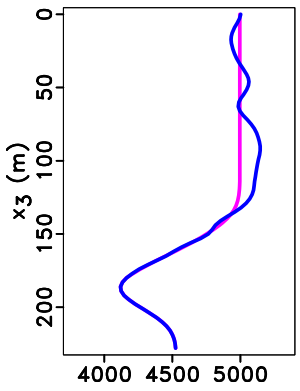

Figure 17 Vertical profiles of the initial (magenta) and inverted (blue) velocity V_{hor} (in m/s) near the centre of the model from Fig. 10.

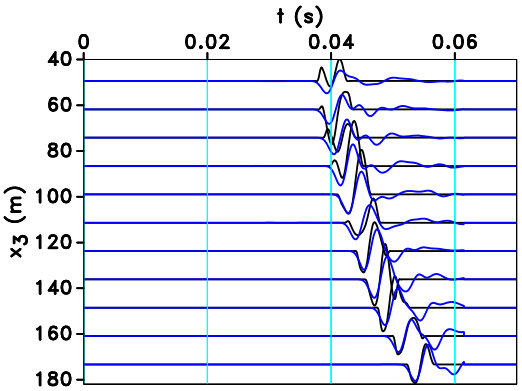

Figure 19 Vertical displacement for one of the microseismic events windowed to include just the P-wave direct arrivals (black lines). The same displacement computed with the inverted parameters V_{hor} and η (blue lines).

needed to take full advantage of 3D anisotropic waveform inversion.

CONCLUSIONS

We presented a 3D elastic waveform-inversion algorithm designed to estimate the gridded parameters V_{hor}, V_{S0}, η and ε responsible for propagation of P- and SV-waves in vertical symmetry axis (VTI) media. The wavefields are modelled with the pseudospectral method that reduces numerical dispersion compared to finite differences without increasing the model size. The waveform inversion (WI) gradient is computed with the adjoint-state method in two modelling simulations.

The algorithm was applied to synthetic microseismic data recorded in three vertical "boreholes" embedded in a layered VTI model. Despite the suboptimal source-receiver aperture, the VTI parameters were recovered in the central part of the model with acceptable accuracy. Improved results can be expected for a more distributed event cloud providing better illumination. To test the algorithm on a heterogeneous model typical for unconventional plays, we introduced two anomalies simulating hydraulic fractures in all four VTI parameters. Although the data coverage is sparse, both anomalies can be identified in the inverted V_{hor}- and V_{S0}-fields; improved fracture delineation can be achieved with a wider source-receiver aperture. We also showed that the inversion remains sufficiently accurate and the fractures can be identified in the presence of moderate band-limited random noise and realistic errors in the event locations.

Finally, we discussed preliminary WI results for a microseismic data set acquired at an unconventional shale reservoir. The goal of this case study was to improve the velocity model obtained using traveltime inversion by fitting the waveforms of the direct P-wave arrivals. Data-conditioning steps such as first-arrival windowing, frequency filtering, and wavelet estimation proved to be essential for application of WI. The algorithm was initially used to invert the P-wave direct arrivals for the parameters V_{hor} and η. Despite the suboptimal data coverage, the objective function was substantially reduced and the inverted model provides a good match for the direct P-arrivals. Ongoing work that includes additional events and shear waves should help in refining the anisotropic velocity field.

ACKNOWLEDGEMENTS

We are grateful to Vladimir Grechka (Marathon Oil) for sharing his insights into various aspects of this research. We thank Ivan Lim (Chevron, formerly CWP) and Vladimir Li (Ikon Science, formerly CWP) for their helpful suggestions. This work was supported by the Consortium Project on Seismic Inverse Methods for Complex Structures at the Center for Wave Phenomena (CWP).

REFERENCES

Aki K. and Richards P.G. 2002. *Quantitative Seismology*. University Science Books, Mill Valley, CA.

Alkhalifah T. and Plessix R. 2014. A recipe for practical full-waveform inversion in anisotropic media: an analytical parameter resolution study. *Geophysics* **79**, R91–R101.

Byrd R.H., Lu P., Nocedal J. and Zhu C. 1995. A limited memory algorithm for bound constrained optimization. *SIAM Journal on Scientific Computing* **16**, 1190–1208.

Cheng J., Alkhalifah T., Wu Z., Zou P. and Wang C. 2016. Simulating propagation of decoupled elastic waves using low-rank approximate mixed-domain integral operators for anisotropic media. *Geophysics* **81**, T63–T77.

Fichtner A., Bunge H.-P. and Igel H. 2006. The adjoint method in seismology: i. Theory. *Physics of the Earth and Planetary Interiors* **157**, 86–104.

Grechka V. and Duchkov A. 2011. Narrow-angle representations of the phase and group velocities and their applications in anisotropic velocity-model building for microseismic monitoring. *Geophysics* **76**, WC127–WC142.

Grechka V. and Heigl W. 2017. *Microseismic Monitoring*. Society of Exploration Geophysicists.

Grechka V., Li Z., Howell B., Garcia H. and Wooltorton T. 2017. High-resolution microseismic imaging. *The Leading Edge* **36**, 822–828.

Grechka V. and Yaskevich S. 2013. Inversion of microseismic data for triclinic velocity models. *Geophysical Prospecting* **61**, 1159–1170.

Grechka V. and Yaskevich S. 2014. Azimuthal anisotropy in microseismic monitoring: a Bakken case study. *Geophysics* **79**, KS1–KS12.

Jarillo Michel O. and Tsvankin I. 2015. Estimation of microseismic source parameters by 2D anisotropic waveform inversion. *Journal of Seismic Exploration* **24**, 379–400.

Jarillo Michel O. and Tsvankin I. 2017. Waveform inversion for microseismic velocity analysis and event location in VTI media. *Geophysics* **82**, WA95–WA103.

Jost M.L. and Herrmann R.B. 1989. A students guide to and review of moment tensors. *Seismological Research Letters* **60**, 37–57.

Kamath N., Tsvankin I. and Díaz E. 2016. *Elastic FWI for VTI media: a synthetic parameterization study*. CWP Project Review Report.

Kamath N., Tsvankin I. and Díaz E. 2017. Elastic full-waveform inversion for VTI media: a synthetic parameterization study. *Geophysics* **82**, C163–C174.

Kim Y., Liu Q. and Tromp J. 2011. Adjoint centroid-moment tensor inversions. *Geophysical Journal International* **186**, 264–278.

Liu Q. and Tromp J. 2006. Finite-frequency kernels based on adjoint methods. *Bulletin of the Seismological Society of America* **96**, 2383–2397.

Maxwell S. 2014. *Microseismic Imaging of Hydraulic Fracturing*. Society of Exploration Geophysicists.

Plessix R.-E. 2006. A review of the adjoint-state method for computing the gradient of a functional with geophysical applications. *Geophysical Journal International* **167**, 495–503.

Stump B.W. and Johnson L.R. 1977. The determination of source properties by the linear inversion of seismograms. *Bulletin of the Seismological Society of America* **67**, 1489.

Sun J., Fomel S., Sripanich Y. and Fowler P. 2016. Recursive integral time extrapolation of elastic waves using lowrank approximation. 86th annual international meeting, SEG, Expanded Abstracts, 4145–4151.

Vavryčuk V. 2007. On the retrieval of moment tensors from borehole data. *Geophysical Prospecting* **55**, 381–391.

Vavryčuk V. and Kühn D. 2012. Moment tensor inversion of waveforms: a two-step time-frequency approach. *Geophysical Journal International* **190**, 1761–1776.

Wuestefeld A., Al-Harrasi O., Verdon J.P., Wookey J. and Kendall J.M. 2010. A strategy for automated analysis of passive microseismic data to image seismic anisotropy and fracture characteristics. *Geophysical Prospecting* **58**, 755–773.

APPENDIX: 3D INVERSION GRADIENT FOR THE PARAMETERS OF TRANSVERSELY ISOTROPIC MEDIA

Following Kamath, Tsvankin and Díaz (2016) and Jarillo Michel and Tsvankin (2017), we describe P- and SV-wave propagation in VTI media by the following four parameters:

$$m_1 = (V_{\rm hor}/V_{{\rm hor},i})^2, \tag{A1}$$

$$m_2 = (V_{\rm S0}/V_{{\rm S0},i})^2, \tag{A2}$$

$$m_3 = 1 + 2\eta\,, \tag{A3}$$

$$m_4 = 1 + 2\varepsilon, \tag{A4}$$

where $V_{{\rm hor},i}$ and $V_{{\rm S0},i}$ are the initial values of the velocities $V_{\rm hor}$ and $V_{\rm S0}$, respectively. Applying the chain rule to equation (3), the derivatives of the objective function for this parameterization that include the dependence on all three coordinates are given by

$$\begin{aligned}\frac{\partial \mathcal{F}}{\partial m_1} = -\rho V_{{\rm hor},i}^2 \int_0^T \Bigg[&\frac{\partial \psi_1}{\partial x_1}\frac{\partial u_1}{\partial x_1} + \frac{\partial \psi_2}{\partial x_2}\frac{\partial u_1}{\partial x_1} + \frac{\partial \psi_1}{\partial x_1}\frac{\partial u_2}{\partial x_2} \\ &+ \frac{\partial \psi_2}{\partial x_2}\frac{\partial u_2}{\partial x_2} + \frac{1}{1+2\varepsilon}\frac{\partial \psi_3}{\partial x_3}\frac{\partial u_3}{\partial x_3} \\ &+ \frac{1}{2}\left(\frac{f}{1+2\varepsilon} + \frac{1}{f(1+2\eta)}\right)\left(\frac{\partial \psi_3}{\partial x_3}\frac{\partial u_1}{\partial x_1} + \frac{\partial \psi_1}{\partial x_1}\frac{\partial u_3}{\partial x_3}\right. \\ &\left. + \frac{\partial \psi_3}{\partial x_3}\frac{\partial u_2}{\partial x_2} + \frac{\partial \psi_2}{\partial x_2}\frac{\partial u_3}{\partial x_3}\right)\Bigg]\,{\rm d}t,\end{aligned} \tag{A5}$$

$$\begin{aligned}\frac{\partial \mathcal{F}}{\partial m_2} = -\rho V_{{\rm S0},i}^2 \int_0^T \Bigg[&\left(\frac{\partial \psi_1}{\partial x_3} + \frac{\partial \psi_3}{\partial x_1}\right)\left(\frac{\partial u_1}{\partial x_3} + \frac{\partial u_3}{\partial x_1}\right) \\ &+ \left(\frac{\partial \psi_2}{\partial x_3} + \frac{\partial \psi_3}{\partial x_2}\right)\left(\frac{\partial u_2}{\partial x_3} + \frac{\partial u_3}{\partial x_2}\right) - \left(\frac{f}{2} + \frac{1}{2f} + 1\right) \\ &\times \left(\frac{\partial \psi_3}{\partial x_3}\frac{\partial u_1}{\partial x_1} + \frac{\partial \psi_1}{\partial x_1}\frac{\partial u_3}{\partial x_3} + \frac{\partial \psi_3}{\partial x_3}\frac{\partial u_2}{\partial x_2} + \frac{\partial \psi_2}{\partial x_2}\frac{\partial u_3}{\partial x_3}\right)\Bigg]{\rm d}t,\end{aligned} \tag{A6}$$

$$\begin{aligned}\frac{\partial \mathcal{F}}{\partial m_3} = \frac{\rho V_{\rm hor}^2}{2f(1+2\eta)^2} \int_0^T \Bigg(&\frac{\partial \psi_3}{\partial x_3}\frac{\partial u_1}{\partial x_1} + \frac{\partial \psi_1}{\partial x_1}\frac{\partial u_3}{\partial x_3} + \frac{\partial \psi_3}{\partial x_3}\frac{\partial u_2}{\partial x_2} \\ &+ \frac{\partial \psi_2}{\partial x_2}\frac{\partial u_3}{\partial x_3}\Bigg)\,{\rm d}t,\end{aligned} \tag{A7}$$

$$\begin{aligned}\frac{\partial \mathcal{F}}{\partial m_4} = \frac{\rho V_{\rm hor}^2}{(1+2\varepsilon)^2} \int_0^T \Bigg[&\frac{\partial \psi_3}{\partial x_3}\frac{\partial u_3}{\partial x_3} + \frac{f}{2}\left(\frac{\partial \psi_3}{\partial x_3}\frac{\partial u_1}{\partial x_1} + \frac{\partial \psi_1}{\partial x_1}\frac{\partial u_3}{\partial x_3}\right. \\ &\left. + \frac{\partial \psi_3}{\partial x_3}\frac{\partial u_2}{\partial x_2} + \frac{\partial \psi_2}{\partial x_2}\frac{\partial u_3}{\partial x_3}\right)\Bigg]\,{\rm d}t,\end{aligned} \tag{A8}$$

$$f \equiv \sqrt{\frac{V_{\rm nmo}^2 - V_{\rm S0}^2}{V_{\rm P0}^2 - V_{\rm S0}^2}};\; V_{\rm nmo} = V_{\rm P0}\sqrt{1+2\delta}. \tag{A9}$$

Here, $\mathbf{u}$ and $\boldsymbol{\psi}$ are the forward and adjoint displacement fields, respectively.

